JOURNAL OF GEOPHYSICAL RESEARCH, VOL. 116, C04023, doi:10.1029/2010JC006520, 2011

Hydraulically controlled front trapping on a tidal flat

Julia C. Mullarney[1] and Stephen M. Henderson[1]

Received 12 July 2010; revised 8 December 2010; accepted 4 January 2011; published 26 April 2011.

[1] We report observations of baroclinic surface fronts in Skagit Bay. The fronts formed repeatedly in very shallow (<0.7 m deep) water along the edge of a tidal channel shortly after the incoming tide flooded the adjacent tidal flat and eventually departed from channel edge as the flood tide progressed. The fronts were surface convergence zones, trapping GPS drifters and other flotsam. Across-front salinity (temperature) jumps were a few practical salinity units (a few degrees) with freshwater on the channel side. Across-front transects of velocity (from mobile and fixed acoustic Doppler current profilers) and density (from mobile and fixed conductivity-temperature-depth profilers) are presented. Composite Froude numbers indicate that supercritical flow over the flats initially held fronts near the channel edge. As flood tide progressed, depth-averaged flow speeds decreased, while internal wave speeds increased, owing to increasing depths and density gradients. Flow over the flats eventually became subcritical, at which point fronts departed from the channel edge. The front then formed the leading edge of a shallow (around 0.3 m thick) freshwater plume which propagated across the flats against the incoming tidal flow. Water was then exchanged between the channel and flats with a channel edge composite Froude number near 0.5, consistent with mixing-induced reduction in channel-flats exchange. The across-channel velocity shear was correlated with the across-channel wind, consistent with a simple eddy viscosity model. Strong winds prevented plume propagation.

Citation: Mullarney, J. C., and S. M. Henderson (2011), Hydraulically controlled front trapping on a tidal flat, *J. Geophys. Res.*, *116*, C04023, doi:10.1029/2010JC006520.

1. Introduction

[2] The meeting of freshwater and saltwater, together with subsequent mixing, plays a critical role in estuarine ecology, and in transport of sediments and pollutants. Surface transitions between freshwater and saltwater masses are often marked by fronts, visible as foam or debris lines, sometimes with different colored water masses on either side of the front [*Largier*, 1992]. These foam lines highlight surface convergence zones with downwelling at the front [*Simpson and Nunes*, 1981; *Nunes and Simpson*, 1985; *Scott*, 1994; *O'Donnell et al.*, 1998; *Marmorino et al.*, 2000; *Marmorino and Trump*, 2004]. In addition to being zones of intense mixing, fronts can be locations of enhanced biological activity [e.g., *Clancy and Epifanio*, 1989; *Tyler and Seliger*, 1978; *Zeldis and Jillett*, 1982]. Many different front configurations have been observed [*O'Donnell*, 1993]. This paper presents observations of hydraulically controlled surface fronts.

[3] Fronts propagate as baroclinic gravity currents, and are advected by underlying barotropic flows. If the barotropic speed exceeds the baroclinic speed ("supercritical flow"), then fronts are advected downstream. If the baroclinic speed exceeds the barotropic speed ("subcritical flow"), then fronts can propagate upstream against the barotropic flow. Flows over estuarine shoals are often supercritical (constriction ensures fast barotropic currents, and shallow depth ensures slow baroclinic propagation) while flow downcurrent of shoals is subcritical. When an incoming flood tide flows from a shoal and into deeper water, a supercritical-subcritical transition (a "hydraulic control point") often traps across-channel surface fronts on the landward side of sills or constrictions. Such across-channel "intrusion fronts" have been observed over a wide range of horizontal scales (several m to tens of km) and vertical scales (m to hundreds of m) [*Farmer and Armi*, 1986; *Largier*, 1992].

[4] We report observations of hydraulically controlled fronts in very shallow (<0.7 m) depths over a tidal flat in Skagit Bay, WA. Unlike across-channel intrusion fronts [*Largier*, 1992; *Thain et al.*, 2004], the fronts we observed stretch along a channel edge, owing to presence of broad flats and channel-oblique tidal currents. As the Skagit Bay flats were flooded by the rising tide, incoming high-density salty water cascaded down into the tidal channel, while surface fronts developed along the channel edge. This contrasts with the spreading of saltwater from the channel to the flats observed and simulated in a narrower estuary with weaker across-channel currents [*Ralston and Stacey*, 2005].

---

[1] School of Earth and Environmental Sciences, Washington State University, Vancouver, Washington, USA.

0148-0227/11/2010JC006520

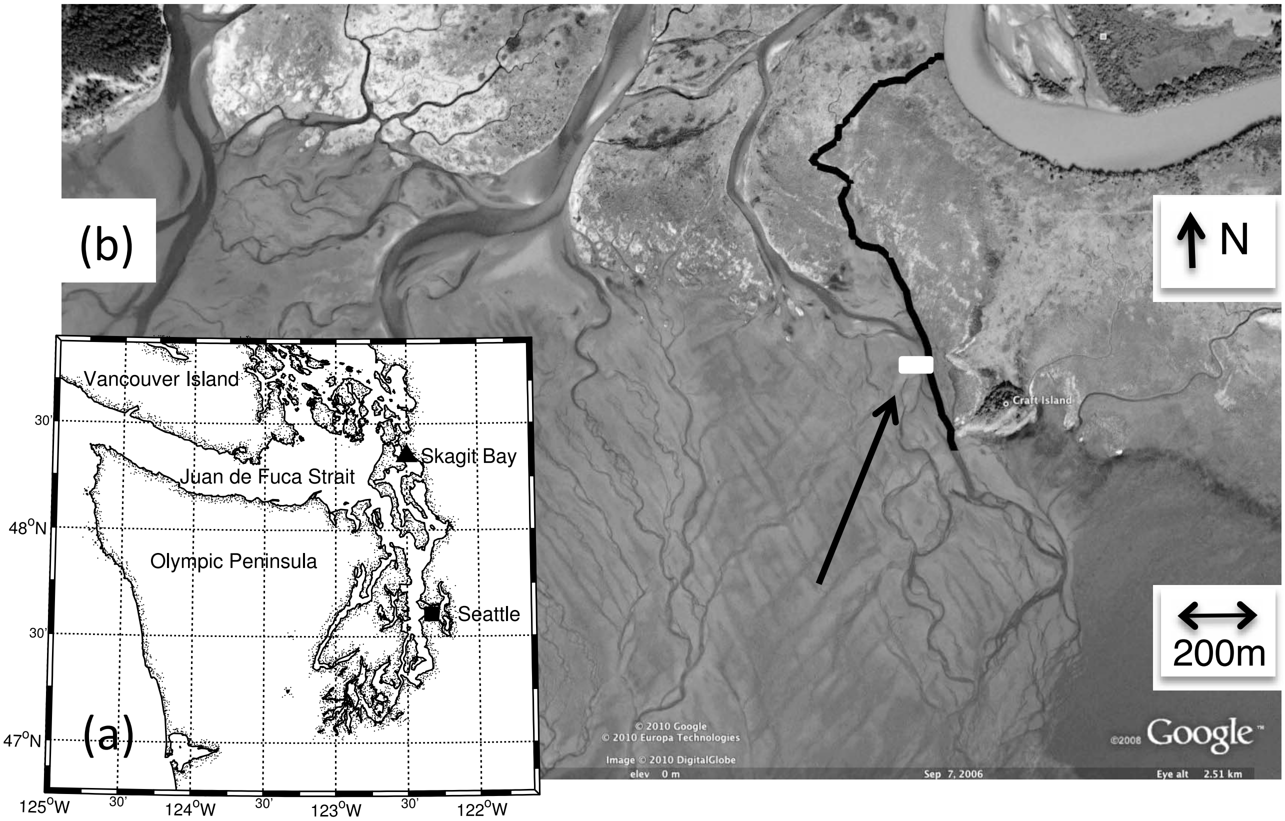

Figure 1. (a) Coastline of Puget Sound showing the location of Skagit Bay. (b) Satellite image of Skagit Bay showing the North Fork of the Skagit River (top right) and the distributary channel (thick black line), which is the focus of this paper. The white box shows the area plotted in Figure 2a. The arrow shows the typical direction of the incoming tidal current. Google Earth imagery (© Google Inc., used with permission) containing imagery from Europa Technologies (© 2010 Europa Technologies) and DigitalGlobe (© 2010 DigitalGlobe).

Owing to the very shallow depths in which channel edge fronts formed, only small (~0.1 ms^{-1}) across-channel velocities were required to ensure supercritical flow over the flats.

[5] After introducing the field site (section 2), instrumentation, and analysis techniques (section 3), we report detailed density and velocity transects across a single front (section 4). Composite Froude numbers indicate that the fronts were hydraulically controlled. As the flood tide progressed, depths increased, currents grew weaker, and flow over the flats became subcritical. At this stage the front departed from the channel edge and propagated as the leading edge of a shallow (<0.3 m deep) surface freshwater plume. Velocity profiles indicate that wind-generated shear can oppose and cancel baroclinic flows (section 5), and long time series show that fronts formed repeatedly during flood tides (section 6). Results are summarized in section 7.

2. Field Site

[6] Skagit Bay is a mesotidal bay within northern Puget Sound, Washington (Figure 1a). The North Branch of the Skagit River enters the eastern, shallow side of the bay. Several distributary channels branch off the river and flow southward through the vegetated salt marsh. Once these distributary channels reach the tidal flats (48.35°N, 122.48°W), they split into a braided network of many shallow subtidal channels. The channels develop and migrate over a timescale of years [*Hood*, 2006]. We focus on the flow in the easternmost distributary channel (marked by the thick black line in Figure 1b), which is characterized by strong flows with maximum flood tide velocities of around 0.5 m s^{-1}. The incoming flood tide approaches from around 200°, flowing across the tidal flats to reach the channel obliquely. This channel-oblique flow contrasts with the more typical channel-parallel flows observed in the absence of tidal flats.

3. Data Acquisition and Processing

[7] High-resolution across-channel transects of velocity, salinity and temperature were resolved during brief (2–4 h) deployments of both mobile and fixed acoustic Doppler current profilers (ADCPs, 2 MHz Nortek Aquadopps), conductivity-temperature (CT) profilers (RBR XR-420s) and a conductivity-temperature-depth (CTD) profiler (RBR XR-620). Each CTD transect took approximately 5 min to complete.

[8] Longer time series (three deployments, each 2–4 weeks) were recorded by fixed CTs and bottom-mounted upward looking ADCPs. ADCPs were distributed in various configurations and occupied six different locations (Figure 2).

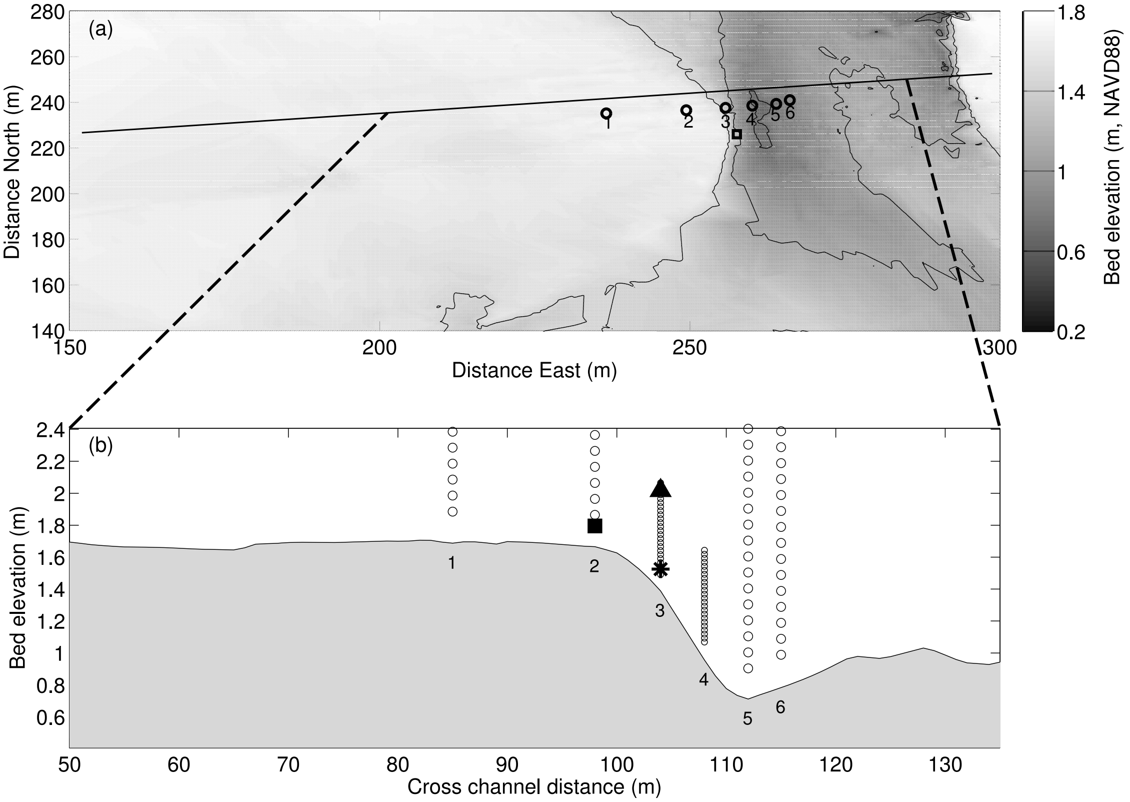

Figure 2. (a) Channel bathymetry (location shown by white square in Figure 1b). Black circles show the locations of stationary ADCPs, and the square shows the location of the fixed conductivity-temperature sensors. The black line shows the across-channel transect (section 3). The weather station was located off the image at (87 m E, 277 m N). (b) Transect showing measurement locations for ADCPs 1 to 6 (instruments 3 and 4 were operating in pulse-coherent mode). Solid symbols show locations of the temperature and salinity measurements during the long-term deployments (section 6) (triangle and star, CT sensors; square, ADCP temperature sensor).

Bathymetry was measured by an RTK GPS survey (precision <0.05 m).

3.1. Prolonged Time Series

[9] Velocity time series were measured by stationary ADCPs (Figure 2), with four operating in standard mode (velocities were recorded in 0.1 m range bins every 20 s and subsequently filtered with a 4 minute moving average) and two operating in pulse-to-pulse coherent mode (0.025 m vertical resolution and 8 Hz time resolution). Owing to side lobe effects and strong acoustic reflections from the surface, velocities in the upper range bin may be biased toward the velocity of water at the surface (as opposed to being a vertically centered mean of the velocities across the range bin). During prolonged deployments, two nearby CT sensors (Figure 2b) measured salinity and temperature approximately 0.1 m and 0.6 m above the bed every 10 s. Atmospheric pressure, wind speed and wind direction were measured 4.2 m above the flats every minute by a weather station about 150 m west of the channel edge (out of the image in Figure 2a at (87 m E, 277 m N)).

3.2. High-Resolution Transects

[10] High-resolution across-channel salinity and temperature transects (continuing onto the flats) were measured at 6 Hz by a CTD profiler. Profiler location was recorded by an i-Blue 887 Mini GPS. Fixed ADCPs (Figure 2) were supplemented by high-resolution (0.025 m, ~0.05 m and 8 Hz vertical, horizontal and temporal resolution) across-channel transects of velocity recorded by a pair of pulse-coherent ADCPs cantilevered in front of a small boat. An upward looking ADCP measured flows within a few (<5) centimeters of the surface, resolving thin (~0.3 m) surface plumes. A downward looking ADCP recorded near-bed velocity profiles, and the 8 Hz measurements of apparent bed motion (relative to the instrument) were used to remove instrument motion and transform velocities measured by mobile instruments into fixed coordinates. Vertical velocities showed evidence of flow disturbance (a few centimeters per second) within 0.1 m of the instruments, and are not presented here. No corresponding evidence of disturbance to horizontal flows was found and horizontal velocities were consistent with those recorded by nearby stationary instruments. Postprocessing of pulse-coherent ADCP data removed, and interpolated over, bins with low (<70%) correlations.

[11] For the mobile downward looking ADCP case, an unwrapping routine removed velocity ambiguities along each beam by (1) minimizing velocity differences between adjacent range bins and (2) subtracting the 8 Hz time series

of apparent along-beam velocity at the bed from all range bins. Condition 2 introduces a requirement that the ADCP "sees" the bed. Given the short range of pulse-coherent profilers, this technique is therefore limited to very shallow water. Wraps were identified in the upward looking mobile ADCP by applying condition 1 above, and minimizing velocity difference between the lowest upward looking bin and the highest downward looking bin. A CT sensor was attached to the ADCPs, and GPS loggers recorded boat location.

[12] Lagrangian tracking of surface flows was provided by GPS drifters. The drifters were close to neutrally buoyant (extending from about 0.08 m below to 0.02 m above the surface).

[13] To facilitate comparison between transects whose along-channel location varied by a few meters, all transects and ADCP profiles were orthogonally projected onto a single line (Figure 2a). Velocities were rotated into along- and across-channel components using an angle of 10° (results were not sensitive to small changes in this angle).

3.3. Froude Number Calculations

3.3.1. Inviscid, Two-Layer Profiles

[14] Inviscid, two-layer flows are supercritical (subcritical) when the composite Froude number,

$$G = \sqrt{\mathrm{Fr}_1^2 + \mathrm{Fr}_2^2} = \sqrt{\frac{u_1^2}{g'h_1} + \frac{u_2^2}{g'h_2}}, \tag{1}$$

exceeds (is less than) one, where Fr_j is the Froude number of layer j (j = 1 for upper layer, j = 2 for lower layer), u_j and h_j are the across-channel velocity and thickness of layer j, and reduced gravity $g' = g\Delta\rho/\rho_2$, where $\Delta\rho = \rho_2 - \rho_1$ is the density difference between the two layers.

[15] We classified one- and two-layer flows using the across-channel velocity profile. The flow was considered to be two layer if the mean across-channel velocity in a lower portion of the water column was positive (roughly eastward) and the mean across-channel velocity in an upper portion was negative. The interface between the layers was defined to be the zero-velocity height. Velocities u_j were defined as the mean in each layer. To permit calculation of Froude numbers in the case of single layer flow, densities ρ_j were calculated as the minimum (j = 1) and the maximum (j = 2) from each profile, although this may bias Fr low.

[16] When h_1 or h_2 are small, G becomes sensitive to small velocities (equation (1)), and evaluation of G from observations (which contain noise and time dependence) becomes problematic. When $h_1 = h_2$ and the water velocity is depth uniform and equal to $\overline{u}$, G reduces to

$$\overline{G} = \frac{2\overline{u}}{\sqrt{g'(h_1 + h_2)}}. \tag{2}$$

$\overline{G}$ does not allow for $h_1 \neq h_2$, or for depth-dependent velocity but, unlike G, can be evaluated from observations even when h_1 or h_2 become very small.

3.3.2. Inviscid Continuous Profiles

[17] Departures from the idealized two-layer profile assumed in section 3.3.1 modify the conditions for critical flow [*Nielsen et al.*, 2004]. To explore the effects of continuous stratification, we calculated the phase speeds of long, inviscid internal wave modes propagating through the measured, continuous velocity and density profiles. Such waves satisfy the shallow water Taylor-Goldstein equation

$$\frac{\partial^2\psi}{\partial z^2} - \left[\frac{1}{(u-c)}\frac{\partial^2 u}{\partial z^2} - \frac{N^2}{(u-c)^2}\right]\psi = 0, \tag{3}$$

where z is elevation, $N^2 = -(g/\rho)\partial\rho/\partial z$ is the squared buoyancy frequency, u is the mean current, $\psi e^{ik(x-ct)}$ is the stream function, k is wave number, c is phase speed, and boundary conditions require $\psi = 0$ at the surface and the bed. We solved (3) numerically using N^2 calculated directly from measured continuous density profiles. To calculate a composite Froude number, u in (3) was set to u_m/G_{cont}, where u_m was the measured velocity profile, and G_{cont} was adjusted until u was just sufficient to prevent the mode zero wave from propagating upstream (in practice, we assumed critical flow had been achieved when the wave speed was reduced below 0.01 ms^{-1}). Therefore, G_{cont} is the ratio between the measured velocity and the velocity (with the same profile shape) of a critical flow. G_{cont} is a generalization of G (equation (1)): if two uniform layers are separated by a very thin layer of very intense stratification then $G_{\mathrm{cont}} \approx G$.

3.3.3. Influence of Mixing

[18] *MacDonald and Geyer* [2005] found critical G values near 1 in observations of a bottom-trapped front on the Fraser River. However, other authors find that turbulent mixing reduces the critical value of G for surface fronts. Based on laboratory and field data, critical Froude numbers have been found to range from 0.1 to 0.55 [*Akiyama and Stefan*, 1984], from 0.1 to 0.7 [*Ford and Johnson*, 1981] and from 0.3 to 0.8 [*Savage and Brimberg*, 1975].

[19] The influence of mixing was examined by *Hogg et al.* [2001] using numerical simulations of controlled exchange flow through a symmetrical constriction between equal reservoirs containing water of differing densities. The degree of mixing between density layers was quantified using the dimensionless interface thickness h_t, calculated as the depth-normalized vertical distance between the $\rho = \rho_0 - 0.4\Delta\rho$ and $\rho = \rho_0 + 0.4\Delta\rho$ isopycnals, where $\rho_0 = 0.5$ ($\rho_{\max} + \rho_{\min}$). For flows with minimal mixing, interfaces were thin, h_t was small, and the simulated dimensionless upper layer flux $q = 2^{1/2}\,Fr_1$ (equation (1)) at the constriction was near the hydraulic prediction q = 1. Strong mixing led to broad interfaces, large h_t, and flows much weaker than predicted by hydraulic theory ($q \ll 1$). In such cases of strong mixing, simulated flows were well predicted by a model balancing friction with baroclinic pressure forces. In intermediate cases with h_t ranging between 0.3 and 0.8, q ranged from 0.8 to 0.5, intermediate between the frictional and inviscid limits (corresponding to G as identified by (1), ranging from 0.8 to 0.5).

[20] The transition between inviscid and frictional behavior is controlled by the vertical:horizontal aspect ratio A, and the turbulent Grashof number $\mathrm{Gr}_T = g'H^3K_\nu^{-2}$ (comparing buoyancy and mixing, where K_ν is the eddy diffusivity). Scaling analysis predicts, and numerical experiments confirm [*Hogg et al.*, 2001], that $h_t \sim 3.4(\mathrm{Gr}_T A^2)^{-1/4}$. Intermediate cases with

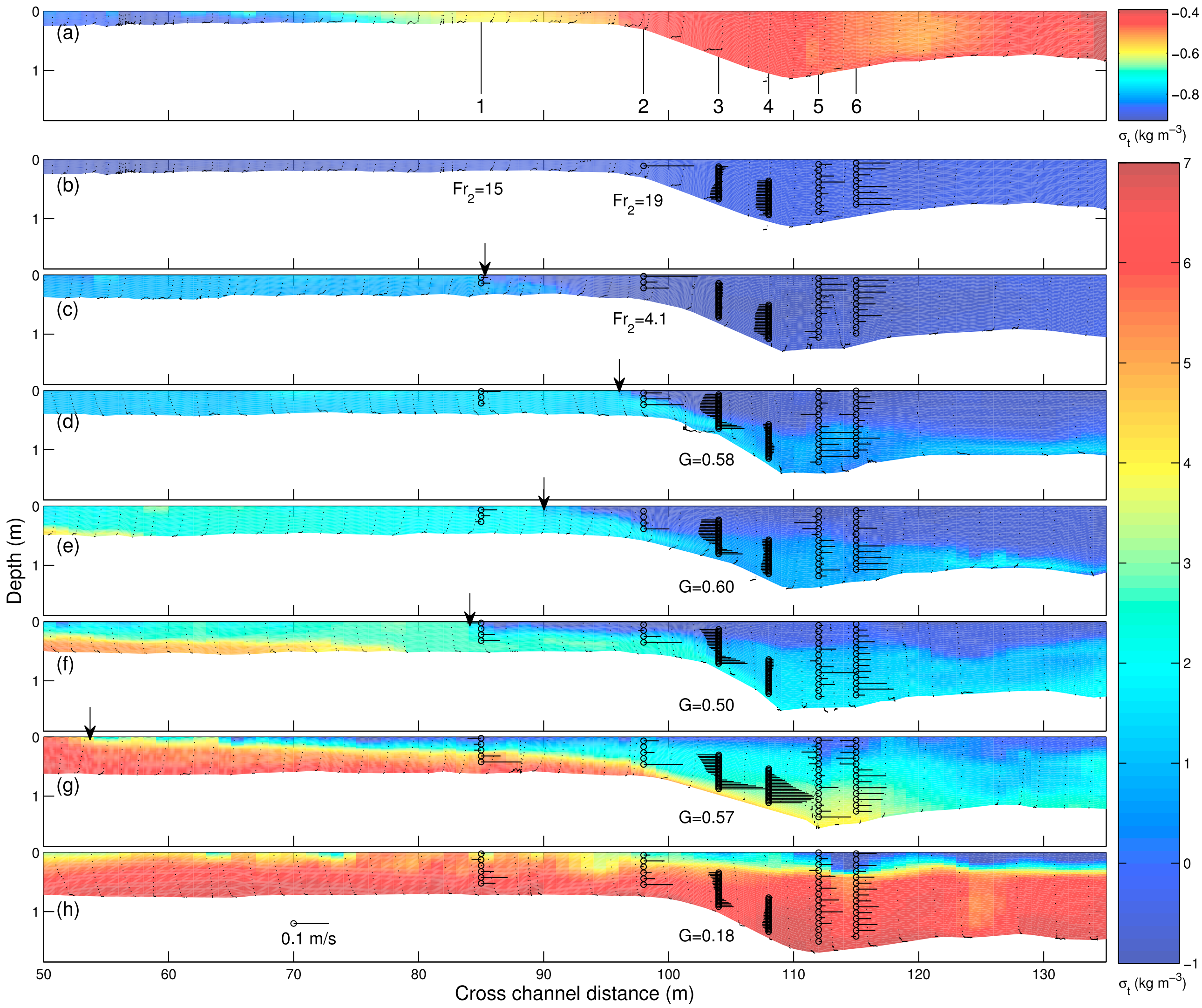

Figure 3. (a–h) Density (σ_t) profiles from a single flood tide in June 2009. Figures 3a and 3b show the same time but with different color scales to illustrate the initial stratification. Figures 3b–3h use the same color scale. Small black dots indicate locations of CTD measurements. Arrows indicate the approximate location of the surface front. The horizontal bars indicate across-channel velocity. Times of transects are (in minutes after the flats were first flooded) 19 (Figures 3a and 3b), 32 (Figure 3c), 38 (Figure 3d), 45 (Figure 3e), 51 (Figure 3f), 60 (Figure 3g), and 82 (Figure 3h). All composite and lower layer densimetric Froude numbers are given in Table 1 with selected values shown here. West is on the left.

h_t ranging between 0.3 and 0.8 correspond to $\mathrm{Gr}_T A^2$ between about 330 and 16,000.

[21] To determine the likely influence of mixing on our results, we calculated h_t from density profiles measured near the channel edge (between x = 95 and x = 100).

4. Case Studies and Across-Channel Transects

[22] Intense baroclinic surface fronts often appeared soon after the incoming tide flooded the channel-adjacent flats. The fronts were clear in infrared observations [*Rinehimer et al.*, 2010] and formed surface convergence zones, trapping GPS drifters and natural flotsam such as foam and seaweed. As the flats were flooded by a rising tide, GPS drifters were advected by surface flows to the channel edge and then propagated along the channel edge in the foam line (not shown). The foam line persisted on the edge of the channel, sometimes with small (~2 m) meanders, for around an hour, aligned roughly with the bathymetric contours. On low-wind days, the front eventually departed from the channel edge and propagated westward over the flats. When the winds were stronger the visible surface signal of the front was destroyed, with surface foam typically advected downwind across the channel and into salt marsh to the east.

[23] On 20 June 2009, winds were moderate (~4 m s^{-1} across channel) and no visible channel edge foam line developed, yet transects (Figure 3) show that a channel edge

Table 1. Lower Layer (Fr_2), Composite (G) Froude Numbers (Section 3), Froude Numbers for a Continuous Stratification (G_{cont}, Section 3.3.2) and Dimensionless Interface Thicknesses (h_t, Section 3.3.3) for the Six ADCP Locations, and Times Corresponding to Figure 3

			Location					
	Time[a]	Parameter	1	2	3	4	5	6
Figures 3a and 3b	18.41	Fr_2	14.85	18.71	0.52	2.65	2.36	3.84
		G						
		G_{cont}						38.09
		h_t					0.02	0.31
Figure 3c	32.18	Fr_2	0.56	4.11	0.33	0.54	0.57	0.93
		G						
		G_{cont}	1.07		6.10	1.07	1.53	0.21
		h_t	0.51			0.38	0.48	0.49
Figure 3d	38.27	Fr_2	0.58	0.62	0.50	0.10	0.42	0.19
		G			0.58	0.12		
		G_{cont}	0.03	1.25	0.46	0.15		0.46
		h_t		0.29	0.27	0.54	0.21	0.30
Figure 3e	45.23	Fr_2	0.30	0.18	0.48	0.10	0.23	0.44
		G			0.60		0.26	
		G_{cont}		0.21	0.64	0.34	0.52	0.46
		h_t	0.56	0.42	0.58	0.42	0.39	0.71
Figure 3f	50.57	Fr_2	0.24	0.58	0.46	0.02	0.08	0.25
		G	0.54	0.58	0.50			
		G_{cont}	0.09		0.34	0.09	1.25	0.40
		h_t	0.47	0.43	0.63	0.68	0.41	0.70
Figure 3g	59.83	Fr_2	0.48	0.20	0.54	0.37	0.16	0.28
		G	0.51		0.57	0.37		0.39
		G_{cont}	0.21	0.40	0.52	0.09	0.34	0.46
		h_t	0.56	0.82	0.91	0.90	0.70	0.69
Figure 3h	82.03	Fr_2	0.21	0.22	0.17	0.03	0.02	0.11
		G			0.18			
		G_{cont}	0.21	0.27	0.09	0.27	0.21	0.40
		h_t	0.58	0.74	0.47	0.34	0.31	0.48

[a] Times are in minutes after the flats were first flooded.

front developed (west is on the left). Figures 3a and 3b show the same transect, but with different color axes to illustrate the early-tide stratification. Figures 3b–3h all use the same color axis, and show the evolution of the front as the incoming tide progressed. Salinity variations over individual transects (which reached 10 practical salinity units (psu)) dominated the density structure, contributing 600% more to density differences than temperature variations (which reached 6°C). Front widths were typically around 5 m with salinity jumps over this region of around 4 psu. The lower layer and composite Froude numbers, together with the dimensionless interface thickness (section 3) at the six ADCP locations are shown in Table 1.

[24] Initially (t = 18.41 min, Figures 3a and 3b) the flow everywhere was supercritical, with particularly large Froude numbers on the flats ($\mathrm{Fr}_2 > 15$), thus density gradients were advected. Along-channel flow was initially faster in the channel than on the flats (Figure 4). As the tide progressed, the Froude number declined until flow in the channel became subcritical ($\mathrm{Fr}_2 < 1$; Table 1) with strengthening stratification on the flats and near the channel edge. Incoming salty water began to cascade down into the channel (Figures 3d–3g). Consequently, cross-channel flows were strongest near the channel bed, unlike along-channel flows which increased monotonically with elevation (not shown). If the near-bed across-channel velocity u_b is baroclinic, then a conservative energy balance predicts

$$g'\Delta z = \frac{u_b^2}{2} \tag{4}$$

(where Δz is the elevation decrease as water cascaded into channel), from which $u_b \sim 0.2$ m/s at ADCP location 3. Turbulent mixing likely accounts for the smaller (0.1 m/s) velocities observed. Therefore, the observed fronts were baroclinic and differ from the barotropic fronts described by *Valle-Levinson et al.* [2000].

[25] During the transition from supercritical to subcritical flow (Figures 3d–3g), two-layer composite Froude numbers (G, section 3.3.1) near the channel edge (from ADCP 3) were G = 0.5–0.6 (mean G = 0.56), consistent with values given by *Savage and Brimberg* [1975], *Ford and Johnson* [1981] and *Akiyama and Stefan* [1984] for hydraulically controlled surface fronts. However, the composite Froude numbers calculated from the pulse-to-pulse coherent Aquadopps are subject to error (likely underestimation) as the ADCP range was too short to measure near-surface velocities.

[26] Composite Froude numbers estimated from inviscid theory using the observed continuous velocity and density profiles (G_{cont}, Table 1 and section 3.3.2) did not differ greatly from two-layer Froude numbers, and during supercritical-subcritical transition (Figures 3d–3g) were 0.34–0.64 (mean 0.49) near the channel edge. Consequently, differences between observed continuous profiles and idealized two-layer profiles were not responsible for reducing G below 1. However, channel edge dimensionless interface thickness (h_t, section 3.3.3) ranged between 0.3 and 0.8, indicating that mixing likely reduced flows to 0.5–0.8 of the inviscid values [*Hogg et al.*, 2001]. We

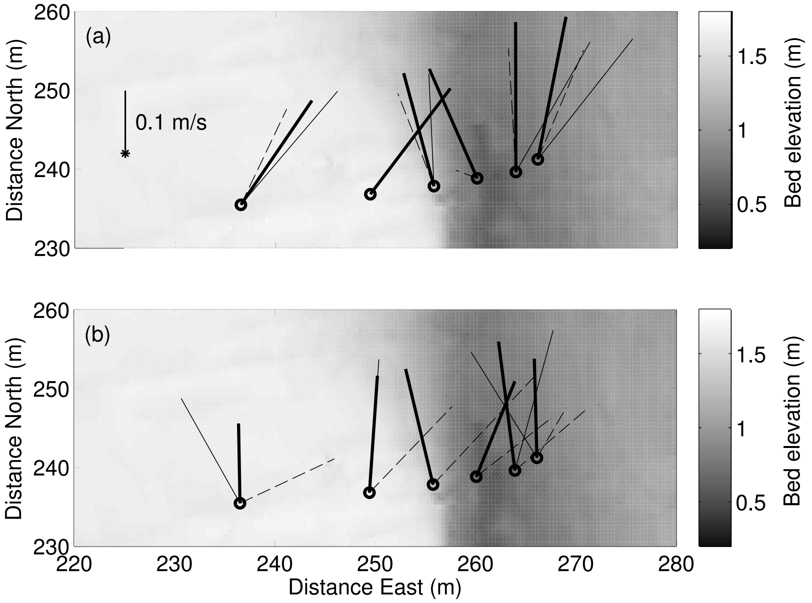

Figure 4. Plan view of velocity vectors (a) 19 and (b) 60 minutes after the flats were flooded (corresponding to Figures 3b and 3g). Bottom velocity is shown by dashed lines, surface velocity is shown by thin solid lines (where available), and depth averaged is shown by thick solid lines.

conclude that mixing was responsible for reducing G values below 1.

[27] As flood tide progressed, depth-averaged flow speeds decreased. Eventually, the front left the channel edge (Figure 3f) and propagated across the flats (Figures 3g and 3h). In the subcritical flow behind the advancing front, G and Fr_2 dropped to less than 0.22.

[28] Straining associated with sheared tidal currents cannot explain formation of the observed front. Tidal straining associated with vertical shear [*Simpson et al.*, 1990] tends to destroy the stratification during flood tide, while straining associated with horizontal shear (channel flow faster than flow over flats) produces channel edge "shear fronts" with salinity gradients opposite to those described here [*Nunes and Simpson*, 1985].

[29] Boat-mounted instruments deployed on 18 August 2009 show that, after leaving the channel edge, the front propagated across the flats as a very thin (0.2–0.3 m) gravity current (Figure 5 shows the front after it had propagated 130 m away from the channel edge). The structure at the leading edge of the plume was similar to the structure of larger plumes, e.g., the 2–3 m deep Connecticut River plume [*O'Donnell et al.*, 2008], and the 5 m deep Chesapeake plume [*Marmorino and Trump*, 2000]. The front at $x = -30$ m is marked by high near-surface backscatter (Figure 5a) and a 0.2 m/s jump in near-surface front-normal velocity (Figure 5b). The base of the fresh plume (0.2 to 0.3 m deep, $x > -30$ m) is marked by a layer of high backscatter (Figure 5a) and shear (Figure 5b). The CT sensor (at about 0.4 m depth) passes beneath the shallow plume and consequently measures the transition to low salinity, temperature and density at the channel edge (x = 97 m), over 100 m from the surface front. The cascading of dense water down into the channel is apparent in the strong near-bed across-channel (Figure 5b) flows for $x > 97$ m.

5. Wind-Driven Flow

[30] An eastward flowing sea breeze developed during most afternoons. The vertical structure of across-channel velocity was wind-dependent. Weak winds allowed development of a simple two-layer flow (labeled 1, Figures 6a and 6d) as the freshwater plume departed from the channel edge and propagated across the flats. Moderate winds (Figures 6b and 6e) from the west-northwest weakened the outward plume flow (labeled 2). Velocities very near (within 0.1–0.2 m of) the surface were sometimes reversed (t = 219–219.05, labeled 3, Figure 6b), and the surface foam line was destroyed, although the freshwater still propagated outward onto the flats in a middle layer below the surface. Stronger winds destroyed the two-layer flow structure and prevented the surface plume from spreading westward from the channel edge (Figures 6c and 6f).

[31] Longer-term records from ADCPs at locations 2 to 5 (Figure 2) show that the mean velocity difference $\overline{\Delta u}$ between upper and lower layers during each flood tide was correlated with the average across-channel wind speed (Figure 7). For one-layer flow, $\overline{\Delta u}$ was given as the mean flow in the top half of the water column minus the mean flow in the bottom half of the water column.

[32] This relationship can be explained by a simple balance between wind and interfacial stress,

$$\rho_a C_{Da} u_a^2 = \rho C_D (\Delta u)^2 \tag{5}$$

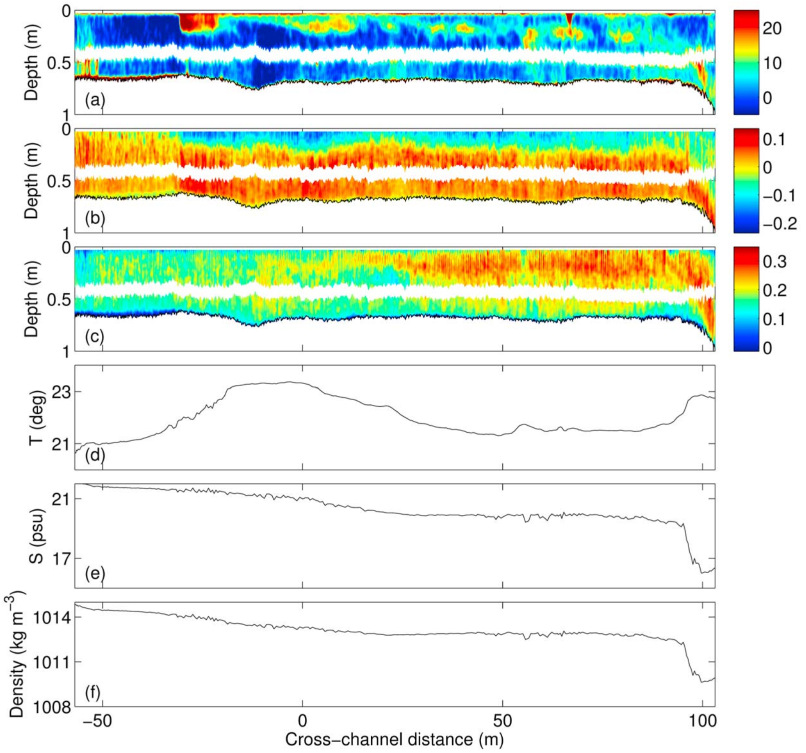

Figure 5. Sections along a westward propagating front of (a) acoustic backscatter (counts), (b) front-normal velocity (m/s), (c) front-parallel velocity (m/s), (d) temperature, (e) salinity, and (f) density (the CT sensor was located at ~0.4 m depth). Black lines in Figures 5a–5c indicate the seabed. The horizontal white band indicates the data gap between upper and lower profiles. The backscatter was the mean of the three beams, with the mean backscatter away from the front subtracted to remove background depth dependence.

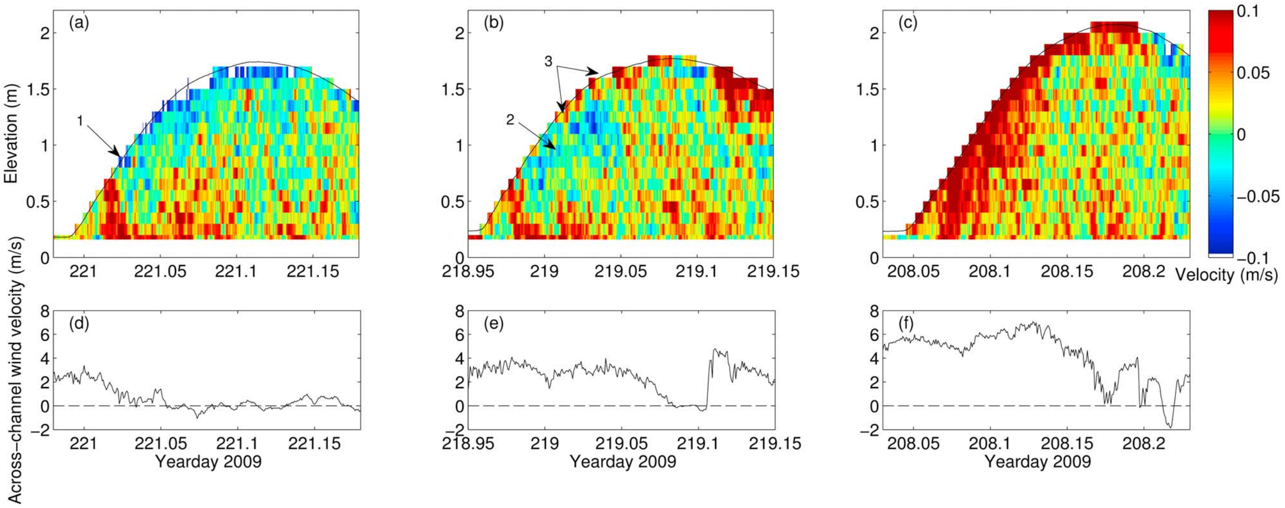

Figure 6. (a–c) Four minute averaged across-channel velocities measured during flood tide by the channel edge ADCP (location 3, Figure 2b) and (d–f) corresponding across-channel wind velocity. Figure 6a shows a clear two-layered shear flow (weak winds). Figure 6b shows a sustained moderate wind, arresting/reversing the surface flow. Figure 6c shows a strong wind day, during which the westward flowing surface plume was prevented from forming. Numbered labels indicate flow features referred to in the text.

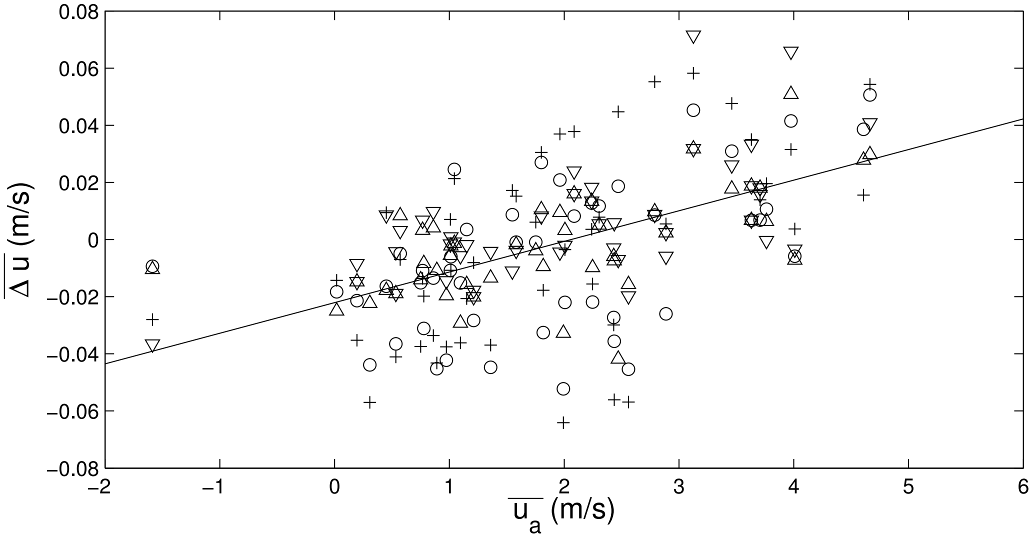

Figure 7. Mean velocity difference between layers over each flood tide versus the corresponding mean across-channel wind velocity. Symbols correspond to locations 2 to 5 (Figure 2b): locations 2 (cross) and 3 (circle) on the flats and locations 4 (triangle) and 5 (inverted triangle) in the channel. The line shows the slope of the first EOF.

(where C_D is a drag coefficient for friction between layers and variables with the subscript a refer to air). Solving for Δu yields

$$\Delta u = \left(\frac{\rho_a C_{Da}}{\rho C_D}\right)^{\frac{1}{2}} u_a. \tag{6}$$

The best fit line (from first EOF) in Figure 7 gives $\Delta u \propto 0.0063 u_a$, which requires

$$C_D = 33 C_{Da} \tag{7}$$

(using ρ = 1000 kg m^{-3}, ρ_a = 1.3 kg m^{-3} in (6)). Observations indicate $C_{Da} \approx 1 \times 10^{-3}$ for winds measured at 10 m elevation [*Gill*, 1982], corresponding to $C_{Da} \approx 1 \times 10^{-3}\,[\log(10/z_0)/\log(4.2/z_0)]^2 = 1.2 \times 10^{-3}$ for our winds measured at 4.2 m using $z_0 = 5 \times 10^{-4}$ m [*Johnson et al.*, 1998]. Substituting into (7) yields an interfacial drag coefficient of C_D = 0.04.

[33] An independent estimate of the interfacial drag coefficient can be obtained from the constant stress model

$$\nu \frac{\partial u}{\partial z} = u_*^2, \tag{8}$$

where z is elevation above bed,

$$u_* = \left(\rho_a C_{Da} u_a^2/\rho\right)^{1/2}, \tag{9}$$

eddy viscosity is approximated by

$$\nu = \kappa u_* \frac{z}{h}(h - z), \tag{10}$$

and Von Karman's constant κ = 0.4. Parameterization (10) neglects enhancement of mixing by breaking surface waves, and is likely an underestimate of ν. The solution to (8) and (10) is

$$u = \frac{u_*}{\kappa}[\log(z) - \log(h - z)] + \text{constant}. \tag{11}$$

Assuming $h_1 = h_2 = h/2$ and approximating $\Delta u \approx u(z = 0.75h) - u(z = 0.25h)$ yields

$$C_D \approx \left[\frac{\kappa}{2\log(3)}\right]^2 \approx 0.03. \tag{12}$$

The strong correlation between shear and wind speed (Figure 7), together with approximate consistency between with the interfacial drag coefficients estimated from observations (C_D = 0.04) and from the eddy viscosity model (C_D = 0.03), indicates that winds played a significant role in generating the observed velocity shear. The best fit line in Figure 7 is offset from zero, likely owing to baroclinic spreading of the surface plume, which also contributes to the observed shear.

6. Temperature and Salinity Time Series

[34] Although the density structure of the front was dominated by salinity, the incoming flow often also had a strong temperature signal. In particular, when the flats were exposed at low tide during the day they were warmed by the sun, and later released the stored heat to the incoming flood tide [*Thomson*, 2010]. Hence, during the early stages of the flood tide, the salty water flowing over the flats was warmer than surface water in the channel. Consequently, the channel edge horizontal temperature difference

$$\Delta T_H = T_f - T_{c,s} \tag{13}$$

was positive on 20 June 2009 (thick line, Figure 8a), where the flats temperature T_f and channel near-surface

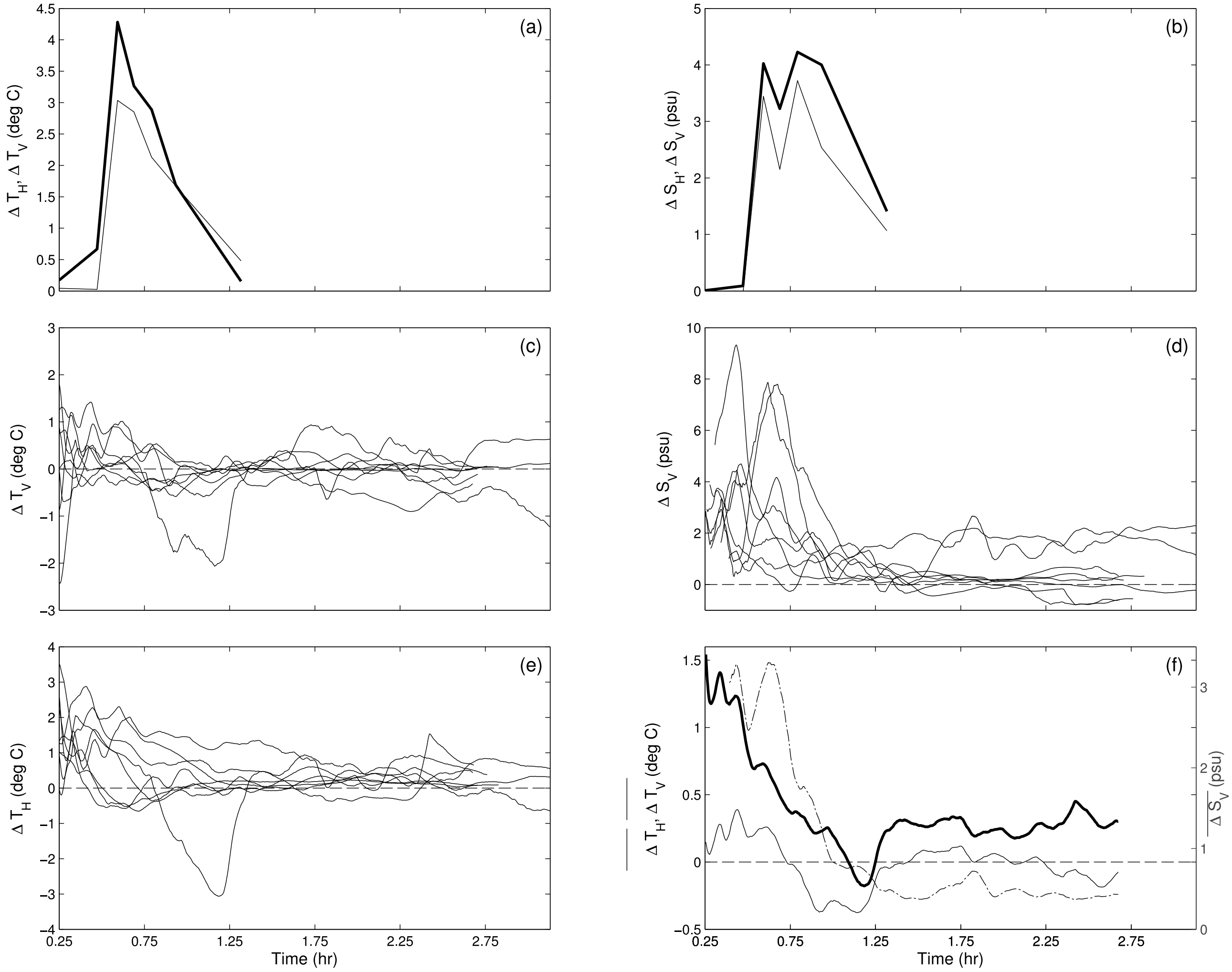

Figure 8. Evolution of across-channel (thick lines) and vertical (thin lines) (a) temperature differences and (b) salinity differences from the flood tide shown in Figure 3. (c) The vertical temperature differences, (d) the vertical salinity differences, and (e) the horizontal temperature differences from longer-term deployments for eight daytime flood tides during which the mean across-channel wind speed was low (<4 m/s). (f) Mean of the horizontal temperature differences (thick line), vertical temperature differences (thin line), and vertical salinity differences (dash-dotted line). Measurements in Figures 8a and 8b were taken from approximately the same locations as those in Figures 8c–8f.

temperature $T_{c,s}$ were measured at the locations of the square and triangle, respectively, in Figure 2b. As the warm salty water cascaded under the near-surface channel water, the channel edge vertical temperature difference

$$\Delta T_V = T_{c,b} - T_{c,s} \tag{14}$$

was positive (thin line, Figure 8a), where the channel near-bed temperature was measured at the location of the star in Figure 2b. Channel edge horizontal and vertical salinity differences ΔS_H and ΔS_V (defined analogously to ΔT_H and ΔT_V) were also positive shortly after the incoming tide flooded the flats (Figure 8b). Channel edge temperature and salinity differences ΔT and ΔS declined after about 45 minutes, as the thin fresh surface layer rose above the upper measurement location.

[35] To identify repeated front formation, long time series of T_f were measured by an ADCP-mounted temperature gauge (black square in Figure 2b). $T_{c,s}$, $T_{c,b}$, $S_{c,s}$ and $S_{c,b}$ were measured by fixed, vertically displaced CTs (black triangle and star in Figure 2b). Using these measurements, channel edge temperature and salinity differences ΔT_H, ΔT_V and ΔS_V were calculated. No instrument was deployed to measure the salinity over the flats S_f, and consequently ΔS_H was not estimated. To ensure strong temperature gradients, only flood tides preceded by at least 6 daylight hours with exposed tidal flats were analyzed (13 cases). Furthermore, cases with mean across-channel winds greater than 4 ms^{-1} are excluded, leaving eight flood tides which met the criteria.

[36] Intense channel edge salinity and temperature differences, resembling those observed on 20 June (Figure 8a) were observed repeatedly (Figures 8c–8f), and usually persisted

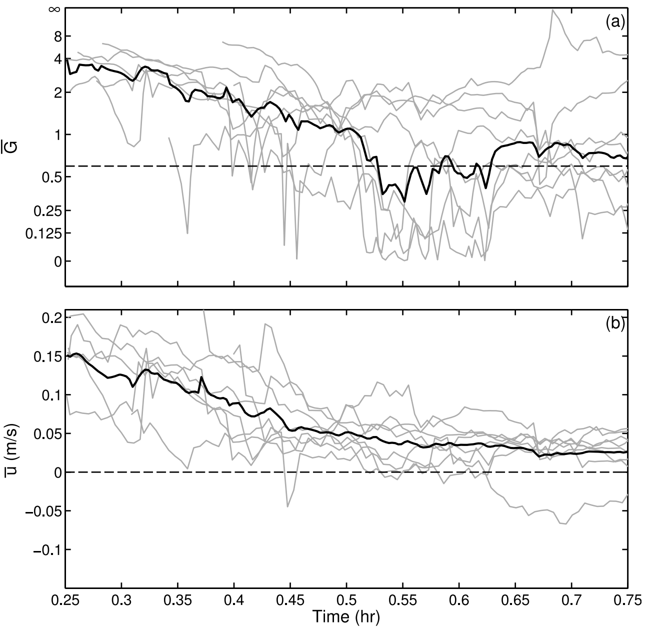

Figure 9. Time series of (a) Froude number $\overline{G}$ (equation (2)) and (b) depth-averaged across-channel velocity $\overline{u}$ for the eight daytime flood tides shown in Figure 8. Note the nonlinear vertical axis in Figure 9a. The thick lines in Figures 9a and 9b indicate geometric and arithmetic means. The horizontal dashed line in Figure 9a indicates $\overline{G} = 0.6$.

0.5–1.5 h. Horizontal temperature changes (1–2°C) exceeded vertical (0–1°C), possibly owing to mixing as water cascaded down into the channel. Salinity differences of 0–10 psu were observed by CTs separated by just 0.5 m (corresponding to $N = 0$–$0.3\ \mathrm{s}^{-1}$).

[37] The vertical temperature and salinity differences shown in Figure 8 were used to calculate time series of the squared Froude number for each tide based on (2) and the depth-averaged across-channel velocity. After the first 45 min, the lower layer thickened to cover both CT sensors (section 4), and ΔS and ΔT declined. To avoid cases where the fresh plume was not measured, $\overline{G}$ is plotted only for 45 min after the flats were flooded. The observed decline of $\overline{G}$ (Figure 9a) often marked a transition from supercritical ($\overline{G} \gtrsim 0.6$) to subcritical ($\overline{G} \lesssim 0.6$) flow over the flats during the first half-hour of flood tide. Owing to the very shallow depths, only very small (~0.1 ms^{-1}) across-channel velocities (Figure 9b) were required for supercritical flow.

7. Summary and Discussion

[38] Surface fronts formed repeatedly along the edge of a tidal channel when depths over the adjacent tidal flat were small (<0.7 m). In such shallow depths, the channel-oblique flow over the flats was often supercritical. As saltwater from the flats plunged beneath the surface front and into the channel the flow became subcritical, indicating hydraulically controlled flows.

[39] The front remained near the channel edge until the composite Froude number dropped below around 0.6. This transition between trapping and propagation is consistent with previous laboratory and field studies of hydraulically controlled surface fronts [*Savage and Brimberg*, 1975; *Ford and Johnson*, 1981; *Akiyama and Stefan*, 1984]. After leaving the channel edge, fronts propagated against the incoming flow, marking the leading edge of thin (0.2–0.3 m thick) freshwater surface plumes. Such plumes are clear in remote infrared images [*Rinehimer et al.*, 2010], but are too thin to be resolved by downward looking ADCP surveys, or by CT sensors just 0.4 m beneath the surface. The composite Froude number remained near 0.5 until the plume had propagated more than 50 m from the channel edge, consistent with a mixing-induced reduction in a hydraulically controlled channel-flats exchange flow.

[40] Winds often opposed plume propagation, contributing significantly to vertical shear. Moderate winds reversed the flow in a thin (0.2 m deep) layer near the surface, whereas stronger winds prevented the plume from forming.

[41] These results show that hydraulically controlled fronts, which are commonly observed in deeper (>1 m) estuaries [*Largier*, 1992; *Thain et al.*, 2004], also occur in very shallow depths (<0.7 m) over tidal flats. Indeed, the extreme shallowness of the flow ensures that even weak (~0.1 m/s) across-channel flows are supercritical. Consequently, the conditions required for hydraulic control are easily met where sufficiently deep channels occur in tidal flat environments. In narrow estuaries, geometric constraints limit the strength of across-channel flows. The breadth of the Skagit Bay tidal flats, combined with the tendency for supercritical flow over the very shallow flats, might explain the contrast between our observations of saltwater cascading into the channel, and more common observations of saltwater spreading from channels to flats [*Ralston and Stacey*, 2005].

[42] **Acknowledgments.** We thank Kassi Dallavis, Chris Eager, Nate Raynor, Drew Becker, Chris Schleffler, and Lisa Hodges for assistance with the field work. Funding was provided by the Office of Naval Research and the State of Washington. We thank Jim Lerczak for the loan of an RBR profiler. Comments from three anonymous referees improved the paper.

References

Akiyama, J., and H. G. Stefan (1984), Plunging flow into a reservoir: Theory, *J. Hydraul. Eng.*, *110*, 484–499.

Clancy, M., and C. E. Epifanio (1989), Distribution of crab larvae in relation to tidal fronts in Delaware Bay, USA, *Mar. Ecol. Prog. Ser.*, *57*, 77–82.

Farmer, D. M., and L. Armi (1986), Maximal two-layer exchange over a sill and through the combination of a sill and contraction with barotropic flow, *J. Fluid Mech.*, *164*, 53–76.

Ford, D. E., and M. C. Johnson (1981), Field observations of density currents in impoundments, in *Proceedings of the Symposium on Surface Water Impoundments: June 2–5, 1980, Minneapolis, Minnesota*, edited by H. G. Stefan, Am. Soc. of Civ. Eng., New York.

Gill, A. E. (1982), *Atmosphere-Ocean Dynamics*, Academic, San Diego, Calif.

Hogg, A. M., G. N. Ivey, and K. B. Winters (2001), Hydraulics and mixing in controlled exchange flows, *J. Geophys. Res.*, *106*, 959–972.

Hood, W. G. (2006), A conceptual model of depositional, rather than erosional, tidal channel development in the rapidly prograding Skagit River Delta (Washington, USA), *Earth Surf. Processes Landforms*, *31*, 1824–1838.

Johnson, H. K., J. Højstrup, H. J. Vested, and S. E. Larsen (1998), On the dependence of sea surface roughness on wind waves, *J. Phys. Oceanogr.*, *28*, 1702–1716.

Largier, J. L. (1992), Tidal intrusion fronts, *Estuaries*, *15*, 26–39.

MacDonald, D. G., and W. R. Geyer (2005), Hydraulic control of a highly stratified estuarine front, *J. Phys. Oceanogr.*, *35*, 374–387.

Marmorino, G. O., and C. L. Trump (2000), Gravity current structure of the Chesapeake Bay outflow plume, *J. Geophys. Res.*, *105*, 28,847–28,861.

Marmorino, G. O., and C. L. Trump (2004), Evolution of the Cape Henry front, *Estuaries*, *27*, 389–396.

Marmorino, G. O., T. F. Donato, M. A. Sletten, and C. L. Trump (2000), Observations of an inshore front associated with the Chesapeake Bay outflow plume, *Cont. Shelf Res.*, *20*, 665–684.

Nielsen, M. H., L. Pratt, and K. Helfrich (2004), Mixing and entrainment in hydraulically driven stratified sill flows, *J. Fluid Mech.*, *515*, 415–443, doi:10.1017/S0022112004000576.

Nunes, R. A., and J. H. Simpson (1985), Axial convergence in a well-mixed estuary, *Estuarine Coastal Shelf Sci.*, *20*, 637–649.

O'Donnell, J. (1993), Surface fronts in estuaries—A review, *Estuaries*, *16*, 12–39.

O'Donnell, J., G. O. Marmorino, and C. L. Trump (1998), Convergence and downwelling at a river plume front, *J. Phys. Oceanogr.*, *28*, 1481–1495.

O'Donnell, J., S. G. Ackleson, and E. R. Levine (2008), On the spatial scales of a river plume, *J. Geophys. Res.*, *113*, C04017, doi:10.1029/2007JC004440.

Ralston, D. K., and M. T. Stacey (2005), Longitudinal dispersion and lateral circulation in the intertidal zone, *J. Geophys. Res.*, *110*, C07015, doi:10.1029/2005JC002888.

Rinehimer, J. P., J. M. Thomson, and C. Chickadel (2010), Sediment-water heat transfer and frontogenesis over a tidal flat, *Eos Trans. AGU*, *91*(26), Ocean Sci. Meet. Suppl., Abstract GO41A-04.

Savage, S. B., and J. Brimberg (1975), Analysis of plunging phenomena in water resource, *J. Hydraul. Res.*, *13*, 187–204.

Scott, C. F. (1994), A numerical study of the interaction of tidal oscillations and non-linearities in an estuary, *Estuarine Coastal Shelf Sci.*, *39*, 477–496.

Simpson, J. H., and R. A. Nunes (1981), The tidal intrusion front: An estuarine convergence zone, *Estuarine Coastal Shelf Sci.*, *13*, 257–266.

Simpson, J. H., J. Brown, J. Matthews, and G. Allen (1990), Tidal straining, density currents, and stirring in the control of estuarine stratification, *Estuaries Coasts*, *13*, 125–132, doi:10.2307/1351581.

Thain, R. H., A. D. Priestley, and M. A. Davidson (2004), The formation of a tidal intrusion front at the mouth of a macrotidal, partially-mixed estuary: A field study of the Dart estuary, UK, *Estuarine Coastal Shelf Sci.*, *61*, 161–172.

Thomson, J. (2010), Observations of thermal diffusivity and a relation to the porosity of tidal flat sediments, *J. Geophys. Res.*, *115*, C05016, doi:10.1029/2009JC005968.

Tyler, M. A., and H. H. Seliger (1978), Annual subsurface transport of a red tide dinoflagellate to its bloom area: Water circulation patterns and organism distributions in the Chesapeake Bay, *Limnol. Oceanogr.*, *23*, 227–246.

Valle-Levinson, A., C. Li, K.-C. Wong, and K. M. M. Lwiza (2000), Convergence of lateral flow along a coastal plain estuary, *J. Geophys. Res.*, *105*, 17,045–17,061.

Zeldis, J. R., and J. B. Jillett (1982), Aggregation of pelagic *Munida gregaria* (Fabricius) (Decapoda, Anomura) by coastal fronts and internal waves, *J. Plankton Res.*, *4*, 839–857.

S. M. Henderson and J. C. Mullarney, School of Earth and Environmental Sciences, Washington State University, 14204 NE Salmon Creek Ave., Vancouver, WA 98686, USA. (juliamullarney@vancouver.wsu.edu)